Performance Study of the Robust Bayesian Regularization Technique for Remote Sensing Imaging in Geophysical Applications

Ivan E. Villalon-Turrubiates, *Member*, *IEEE*, and Adalberto Herrera-Nuñez, *Student Member, IEEE*
Department of Computer Sciences and Engineering
University of Guadalajara Campus Los Valles
Guadalajara-Ameca Highway Km. 45.5, 46600, Ameca Jalisco, Mexico
Phone: (+52) 3757580148 ext. 7267, E-mail: villalon@ieee.org, herrera-nunez@ieee.org

***Abstract*—In this paper, a performance study of a methodology for reconstruction of high-resolution remote sensing imagery is presented. This method is the robust version of the Bayesian regularization (BR) technique, which performs the image reconstruction as a solution of the ill-conditioned inverse spatial spectrum pattern (SSP) estimation problem with model uncertainties via unifying the Bayesian minimum risk (BMR) estimation strategy with the maximum entropy (ME) randomized a priori image model and other projection-type regularization constraints imposed on the solution. The results of extended comparative simulation study of a family of image formation/enhancement algorithms that employ the RBR method for high-resolution reconstruction of the SSP is presented. Moreover, the computational complexity of different methods are analyzed and reported together with the scene imaging protocols. The advantages of the remote sensing imaging experiment (that employ the BR-based estimator) over the cases of poorer designed experiments (that employ the conventional matched spatial filtering as well as the least squares techniques) are verified trough the simulation study. Finally, the application of this estimator in geophysical applications of remote sensing imagery is described.**

Keywords*—*Bayesian estimation; regularization; remote sensing; radar imaging; spatial spectrum pattern.

I. Introduction

Numerical reconstructive image processing is now a mature and well developed research field, presented and detailed in many works, ([1] thru [27] and the references therein). Although the existing theory offers a manifold of statistical and descriptive regularization techniques for reconstructive imaging in many application areas there still remain some unresolved crucial theoretical-level and computational-level problems related to large scale sensor array or synthesized array real-time reconstructive image processing. In this study, we provide a performance study of the robust Bayesian regularization (BR) paradigm for high-resolution remote sensing image formation and enhancement/ reconstruction. The RBR technique (developed in [7], [8], [25]) performs image reconstruction as a solution of the ill-conditioned inverse spatial spectrum pattern (SSP) estimation problem with model uncertainties via unifying the Bayesian minimum risk (MR) estimation strategy with the maximum entropy (ME) randomized a priori image model that incorporates the projection-type regularization constraints imposed on the solution.

The BR method is inferred from a descriptive and statistical constrained optimization paradigm, therefore, we examine how this method leads to a technique that may be further transformed into a new computationally more efficient robust adaptive imaging method that enable one to derive efficient and consistent estimates of the SSP. The principal innovative contribution of this study may be briefly summarized as follows:

- Development of the robust version of the Bayesian regularization technique (RBR) via alleviating the ill-poseness of the nonlinear adaptive operator inversions in the overall image reconstruction procedures.
- Design of an efficient computational algorithm that perform robust adaptive spatial processing for enhanced remote sensing (RS) image formation in a virtually real computational time.
- Comparative analysis of the operational computational structure and performance of the RBR method and related algorithms.

The goal of this study is to address and discuss the computational efficiency of the RBR approach for high-resolution remote sensing imaging for geophysical applications as an ill-conditioned inverse problem of estimating the SSP of the wavefield sources scattered from the probing surface (referred to as the remote sensing image).

Moreover, the results of extended comparative simulation studies of the family of the BR-related SSP estimation algorithms are presented using the Matlab software as simulation tools that provide efficiency and flexibility in performing all simulation experiments.

II. Problem Model

Consider a remote sensing experiment performed with a coherent array imaging radar that is traditionally referred to as radar imaging (RI) problem ([6] – [9]). The measurement sensor data wavefield $u(\mathbf{y}) = s(\mathbf{y}) + n(\mathbf{y})$ modeled as a

superposition of the echo signals s and additive noise n is assumed to be available for observations and recordings within the prescribed time-space observation domain $Y \ni \mathbf{y}$, where $\mathbf{y} = (t, \mathbf{p})^{\mathrm{T}}$ defines the time-space points in the observation domain $Y = T \times P$.

A. Remote sensing problem model

The model of the observation wavefield u is specified by the linear stochastic equation of observation of operator form:

$$u = Se + n; \quad e \in \mathrm{E}; \quad u, n \in \mathrm{U}; \; S: \mathrm{E} \to \mathrm{U} \tag{1}$$

on the Hilbert signal spaces E and U with the metric structures induced by the inner products,

$$[e_1, e_2]_{\mathrm{E}} = \int_X e_1(\mathbf{x}) e_2^*(\mathbf{x}) d\mathbf{x} \quad \text{and} \quad [u_1, u_2]_{\mathrm{U}} = \int_Y u_1(\mathbf{y}) u_2^*(\mathbf{y}) d\mathbf{y}\,, \tag{2}$$

respectively, where asterisk stands for complex conjugate. In (1), the S is referred to as the regular signal formation operator (SFO). It defines the transform of random scattered signals $e(\mathbf{x}) \in \mathrm{E}(X)$ distributed over the remotely sensed scene $X \ni \mathbf{x}$ into the echo signals $(Se(\mathbf{x}))(\mathbf{y}) \in \mathrm{U}(Y)$ over the time-space observation domain $Y = T \times P$; $t \in T$, $\mathbf{p} \in P$. In the functional terms [6], [9], such a transform is referred to as the operator $S: \mathrm{E} \to \mathrm{U}$ that maps the scene signal space E onto the observation data signal space U. This operator model (1) in the conventional integral form [6] may be rewritten as

$$u(\mathbf{y}) = \int_X S(\mathbf{y}, \mathbf{x})\, e(\mathbf{x})\, d\mathbf{x} + n(\mathbf{y})\,, \tag{3}$$

$$e(\mathbf{x}) = e(f; \boldsymbol{\rho}, \boldsymbol{\theta}) = \int_F e(t; \boldsymbol{\rho}, \boldsymbol{\theta}) \exp(-\mathrm{i}2\pi f t)\, dt \tag{4}$$

where the functional kernel $S(\mathbf{y}, \mathbf{x})$ of the SFO S given by (1) defines the signal wavefield formation model [9], [11]. Following the multi-scale array radar remote sensing (RS) problem phenomenology [6], [9], we adopt here an incoherent model of the backscattered field $e(\mathbf{x})$ in the frequency-space observation domain $X = F \times R = F \times P \times \Theta$, i.e. over the slant range $\boldsymbol{\rho} \in P$ and azimuth angle $\boldsymbol{\theta} \in \Theta$ domains, respectively. It is naturally inherent to the RS imaging experiments ([7], [8], [11]) to consider the phasor $e(f, \mathbf{r})$ in (3) to be an independent random variable at each frequency f, and spatial coordinates $\mathbf{r}$, $\boldsymbol{\theta}$ with the zero mean value and δ-form correlation function, $R_e(f, f'; \mathbf{r}, \mathbf{r}') = \langle e(f, \mathbf{r}) e^*(f', \mathbf{r}') \rangle = B(f, \mathbf{r}) \delta(f - f') \delta(\mathbf{r} - \mathbf{r}')$ that enables one to introduce the following definition of the SSP of the wavefield sources distributed in the RS observation environment [9], [27]

$$B(\mathbf{r}) = Aver^{(2)}\{e(\mathbf{r})\} = \int_F \left\langle |e(f, \mathbf{r})|^2 \right\rangle |H(f)|^2\, df; \quad \mathbf{r} \in R. \tag{5}$$

Here, $\langle \cdot \rangle$ represents the ensemble averaging operator, while $Aver^{(2)}$ is referred to as the second order statistical averaging operator defined by (5), $H(f)$ represents the given transfer function of the radar receive channels. In the conventional radar imaging setting ([9], [18], [21]), the initial RS imaging problem is to form an estimate $\hat{B}(\mathbf{x})$ of the SSP distribution $B(\mathbf{r})$ over the remotely sensed scene $R \ni \mathbf{r}$ by processing whatever values of measurements of the data field, $u(\mathbf{y})$; $\mathbf{y} \in Y$, are available. Following the RS data analysis methodology ([1], [2], [20], [22]) any particular physical signature of interest $\hat{\Lambda}(\mathbf{x})$ could be extracted from the reconstructed RS image $\hat{B}(\mathbf{x})$ applying the so-called deterministic signature extraction operator Λ. Hence, the particular RS signature (RSS) is mapped applying Λ to the reconstructed image, i.e.

$$\hat{\Lambda}(\mathbf{x}) = \Lambda(\hat{B}(\mathbf{x})). \tag{6}$$

Taking into account the RSS extraction model (6), we can reformulate now the RSS reconstruction problem as follows: to map the reconstructed particular RSS of interest $\hat{\Lambda}(\mathbf{x}) = \Lambda(\hat{B}(\mathbf{x}))$ over the observation scene $X \ni \mathbf{x}$ via post-processing whatever available values of the reconstructed scene image $\hat{B}(\mathbf{x})$; $\mathbf{x} \in X$.

B. Numerical model

Viewing it as an approximation problem leads one to the projection concept for a transformation of the continuous data field $u(\mathbf{y})$ to the $M \times 1$ vector $\mathbf{U} = (U_1, \ldots, U_M)^{\mathrm{T}}$ of sampled spatial-temporal data recordings. The M-d observations in the terms of projections [7], [8] can be expressed as

$$u_{(M)}(\mathbf{y}) = (P_{\mathrm{U}(M)} u)(\mathbf{y}) = \sum_{m=1}^{M} U_m \varphi_m(\mathbf{y}) \tag{7}$$

with coefficients $\{U_m = [u, h_m]_{\mathrm{U}}\}$ where $P_{\mathrm{U}(M)}$ represents a projector onto the M-d subspace

$$\mathrm{U}_{(M)} = P_{\mathrm{U}(M)} \mathrm{U} = \mathrm{Span}\{\phi_m(\mathbf{y})\} \tag{8}$$

uniquely defined by a set of the orthogonal functions $\{\phi_m(\mathbf{y}) = \|h_m(\mathbf{y})\|^{-2} h_m(\mathbf{y}); \; m = 1, \ldots, M\}$ that are related to $\{h_m(\mathbf{y})\}$ as a dual basis in $\mathrm{U}_{(M)}$. In the observation scene

$X \ni \mathbf{x}$, the discretization of the scattering field $e(\mathbf{x})$ is traditionally performed over a $Q \times N$ rectangular grid where Q defines the dimension of the grid over the horizontal (azimuth) coordinate x_1 and N defines the grid dimension over the orthogonal coordinate x_2 (the number of the range gates projected onto the scene). The discretized complex scattering function is represented by coefficients $E_k = \mathrm{E}_{(q,n)} = [e, g_k]_{\mathrm{E}} = \int_X e(\mathbf{x}) g_k(\mathbf{x}) d\mathbf{x}$; $k = 1,\ldots, K = Q \times N$, of it decomposition over the grid composed of such identical shifted rectangular functions $\{g_k(\mathbf{x}) = g_{(q,n)}(\mathbf{x}) = 1$ if $\mathbf{x} \in \rho_{(q,n)}(\mathbf{x}) = \mathrm{rect}_{(q,n)}(x_1, x_2)$ and $g_k(\mathbf{x}) = 0$ for other $\mathbf{x} \notin \rho_{(q,n)}(\mathbf{x})$ for all $q = 1, \ldots, Q$; $n = 1, \ldots, N$; $k = 1, \ldots, K = Q \times N\}$. Hence, the K-d approximation of the scattering field becomes

$$e_{(K)}(\mathbf{x}) = (P_{\mathrm{E}(K)} e)(\mathbf{x}) = \sum_{k=1}^{K} E_k g_k(\mathbf{x}) \tag{9}$$

where $P_{\mathrm{E}(K)}$ represents a projector onto such K-d signal approximation subspace

$$\mathrm{E}_{(K)} = P_{\mathrm{E}(K)} \mathrm{E} = \mathrm{Span}\{g_k(\mathbf{x})\} \tag{10}$$

spanned by K orthogonal grid functions (pixels) $\{g_k(\mathbf{x})\}$. Using such approximations, it is possible to proceed from the operator form (4) to its conventional numerical form

$$\mathbf{U} = \mathbf{S}\,\mathbf{E} + \mathbf{N}, \tag{11}$$

where $\mathbf{U}$, $\mathbf{N}$ and $\mathbf{E}$ define the vectors composed of the coefficients U_m, N_m and E_k of the finite-dimensional approximations of the fields u, n and e, respectively, and $\mathbf{S}$ is the matrix-form representation of the SFO with elements $\{S_{mk} = [Sg_k, h_m]_{\mathrm{U}} = \int_Y (Sg_k(\mathbf{x}))(\mathbf{y}) h_m^*(\mathbf{y}) d\mathbf{y}$; $k = 1, \ldots, K$; $m = 1, \ldots, M\}$ [6]. Zero-mean Gaussian vectors $\mathbf{E}$, $\mathbf{N}$ and $\mathbf{U}$ in (11) are characterized by the correlation matrices, $\mathbf{R}_{\mathbf{E}}$, $\mathbf{R}_{\mathbf{N}}$ and $\mathbf{R}_{\mathbf{U}} = \mathbf{S}\mathbf{R}_{\mathbf{E}}\mathbf{S}^{+} + \mathbf{R}_{\mathbf{N}}$, respectively, where superscript + defines the Hermitian conjugate when it stands with a matrix or a vector. Because of the incoherent nature of the scattering field $e(\mathbf{x})$, the vector $\mathbf{E}$ has a diagonal correlation matrix, $\mathbf{R}_{\mathbf{E}} = \mathrm{diag}(\mathbf{B}) = \mathbf{D}(\mathbf{B})$, in which the $K \times 1$ vector of the principal diagonal $\mathbf{B}$ is composed of elements $B_k = \langle E_k E_k^* \rangle$; $k = 1, \ldots, K$. This vector $\mathbf{B}$ is referred to as a vector-form representation of the SSP. Using the definition (6) the K-d approximation of the desired RS signature estimate $\hat{\Lambda}_{(K)}(\mathbf{x})$ as a continuous function of $\mathbf{x} \in X$ over the probing scene X is now expressed as

$$\hat{\Lambda}_{(K)}(\mathbf{x}) = \mathrm{est}\{\Lambda \langle |e_{(K)}(\mathbf{x})|^2 \rangle\} = \sum_{k=1}^{K} \Lambda(\hat{B}_k) g_k(\mathbf{x}); \quad \mathbf{x} \in X. \tag{12}$$

Analyzing (12), one may deduce that in every particular measurement scenario one has to derive the estimate $\hat{\mathbf{B}}$ of a vector-form approximation of the SSP that uniquely defines via (12) the approximated continuous pixel-format reconstructed map $\hat{\Lambda}_{(K)}(\mathbf{x})$ of the desired RS signature distributed over the observed scene $X \ni \mathbf{x}$. Hence, the vector

$$\hat{\mathbf{\Lambda}} = \mathrm{vec}\{\Lambda(\hat{B}_k); k = 1, \ldots, K\} \tag{13}$$

represents the numerical model of the reconstructed RS signature (RSS) in the conventional pixel format. Thus, the desired continuous-form RSS is uniquely reconstructed from the estimate $\hat{\mathbf{B}}$ of the SSP vector via (12).

C. Experiment-design considerations

The experiment design (ED) aspects of the problem at hand implies the analysis of how to choose the basis functions $\{g_k(\mathbf{r})\}$ that span the signal representation subspace $\mathrm{E}_{(K)} = P_{\mathrm{E}(K)}\mathrm{E} = \mathrm{Span}\{g_k\}$ for a given observation subspace $\mathrm{U}_{(M)} = \mathrm{Span}\{\varphi_m\}$ ([6], [8], [12]). Here, we formalize such the ED considerations via imposing the metrics structure in the solution space defined by the inner product

$$\|\mathbf{B}\|^2_{\mathrm{B}(K)} = [\mathbf{B}, \mathbf{M}\mathbf{B}] \tag{14}$$

where $\mathrm{B}(K)$ represents the so-called correctness convex solution set [6], and $\mathbf{M}$ is referred to as the metrics inducing operator. Hence, the selection of $\mathbf{M}$ provides additional geometrical ED degrees of freedom of the problem model. In this study, we specify the model for $\mathbf{M}$ that corresponds to the numerical approximation of the Tikhonov's stabilizer of the second order [6]. Next, the projection-type a priori information is incorporated, in which case the SSP vector $\mathbf{B}$ satisfies the linear constraint equation

$$\mathbf{G}\mathbf{B} = \mathbf{C}, \quad \text{i.e. } \mathbf{G}^{-}\mathbf{G}\mathbf{B} = \mathbf{B}_P \tag{15}$$

where $\mathbf{B}_P = \mathbf{G}^{-}\mathbf{C}$ and $\mathbf{G}^{-}$ is the Moore-Penrose pseudoinverse of a given projection constraint operator $\mathbf{G}$: $\mathrm{B}_{(K)} \to \mathrm{B}_{(Q)}$, and the constraint vector $\mathbf{C} \in \mathrm{B}_{(Q)}$ and the constraint subspace $\mathrm{B}_{(Q)}$ ($Q < K$) are assumed to be given [8]. In (15), the constraint operator $\mathbf{G}$ projects the portion of the unknown SSP onto the subspace where the SSP values are fixed by $\mathbf{C}$. In practice, such limitations may specify also the system calibration [15].

III. Bayesian Regularization Method

The robust numerical version of the Bayesian-regularization (BR) method for reconstruction of the power spatial spectrum pattern (SSP) of the wave field scattered from a remotely sensing scene (that is referred to as a

desired RS image) given a finite set of array radar signal recordings was developed originally in [7]. Since the SSP estimation is in essence a nonlinear numerical inverse problem, the proposition in [7] was to alleviate the problem ill-poseness by developing the robust version of the Bayesian estimation strategy [14] via performing the non adaptive approximations of the reconstructive operators that incorporate the non trivial metrics considerations for designing the proper solution space and different regularization constraints imposed on a solution. The estimator that produces the high-resolution optimal estimate $\hat{\mathbf{B}}$ of the SSP vector via processing the M-d data recordings $\mathbf{U}$ applying the BR estimation strategy that incorporates also nontrivial a priori geometrical and projection-type model information was developed in [7] and [8]. Such optimal BR estimate of the SSP is given by the nonlinear equation

$$\hat{\mathbf{B}} = \mathbf{B}_P + \mathbf{P}\mathbf{B}_0 + \mathbf{W}(\hat{\mathbf{B}})\{\mathbf{V}(\hat{\mathbf{B}}) - \mathbf{Z}(\hat{\mathbf{B}})\}. \quad (16)$$

In (16), the constraint $\mathbf{B}_P$ is specified by (15) and $\mathbf{B}_0$ represents the a priori SSP distribution to be considered as a zero step approximation to the desires SSP estimate $\hat{\mathbf{B}}$.

The sufficient statistics (SS) vector $\mathbf{V}(\hat{\mathbf{B}}) = \{\mathbf{F}(\hat{\mathbf{B}})\mathbf{U}\mathbf{U}^{+}\mathbf{F}^{+}(\hat{\mathbf{B}})\}_{\text{diag}}$ is formed via applying to the measured data vector $\mathbf{U}$, the solution-dependent SS formation operator [7]

$$\mathbf{F} = \mathbf{F}(\hat{\mathbf{B}}) = \mathbf{D}(\hat{\mathbf{B}})(\mathbf{I} + \mathbf{S}^{+}\mathbf{R}_{\mathbf{N}}^{-1}\mathbf{S}\mathbf{D}(\hat{\mathbf{B}}))^{-1}\mathbf{S}^{+}\mathbf{R}_{\mathbf{N}}^{-1}. \quad (17)$$

The SS shift vector in (16) is defined as $\mathbf{Z}(\hat{\mathbf{B}})$ [7], and the solution-dependent smoothing-projection window operator

$$\mathbf{W}(\hat{\mathbf{B}}) = \mathbf{P}_{\mathbf{W}}\mathbf{\Omega}(\hat{\mathbf{B}}) \quad (18)$$

is composed of the projector

$$\mathbf{P}_{\mathbf{W}} = (\mathbf{I} - \mathbf{G}^{-}\mathbf{G}) \quad (19)$$

and the solution dependent smoothing window

$$\mathbf{\Omega}(\hat{\mathbf{B}}) = [\text{diag}(\{\mathbf{S}^{+}\mathbf{F}^{+}\mathbf{F}\mathbf{S}\}_{\text{diag}}) + \hat{\alpha}\,\mathbf{D}^{2}(\hat{\mathbf{B}})\mathbf{M}(\hat{\mathbf{B}})]^{-1}, \quad (20)$$

in which the regularization parameter $\hat{\alpha}$ is to be adaptively adjusted using the system calibration data [7]. The resulting BR-optimal estimate in the numerical format is given by

$$\hat{\mathbf{B}}_{BR} = \mathbf{B}_P + \mathbf{P}\mathbf{B}_0 + \mathbf{W}(\hat{\mathbf{B}})\{\mathbf{V}(\hat{\mathbf{B}}) - \mathbf{Z}(\hat{\mathbf{B}})\}. \quad (21)$$

Because of the non-linearity and complexity of the solution-dependent K-d operator inversions needed to be performed to compute the SS $\mathbf{V}(\hat{\mathbf{B}})$, the window $\mathbf{W}(\hat{\mathbf{B}})$ and SS shift $\mathbf{Z}(\hat{\mathbf{B}})$, the computational load of such optimal BR estimator (16) and (21) developed originally in [7] is extremely high to address that as a practically realizable estimator of the SSP and RSS.

A. BR-related robust spatial filtering technique

The robustification scheme for real-time implementation of the BR estimator (16) and (21) enables one to reduce drastically the computation load of the image formation procedure without substantial degradation in the resolution and overall image performances. The robustified version of the BR estimator given by (16) is referred to as the robust BR reconstructive filtering (RBR) method. This method is performed via roughing $\mathbf{P}_{\mathbf{W}} = \mathbf{I}$ and approximating both the SS formation operator $\mathbf{F}(\hat{\mathbf{B}})$ and the smoothing window $\mathbf{\Omega}(\hat{\mathbf{B}})$ in (16) by roughing $\mathbf{D}(\hat{\mathbf{B}}) \approx \mathbf{D} = b_0\mathbf{I}$, where b_0 represents the expected a priori image grey level [7]. Hence, the robustified SS formation operator

$$\mathbf{F} = \mathbf{A}^{-1}(\rho)\mathbf{S}^{+} \quad \text{with} \quad \mathbf{A}(\rho) = \mathbf{S}^{+}\mathbf{S} + \rho^{-1}\mathbf{I} \quad (22)$$

becomes the regularized inverse of the SFO $\mathbf{S}$ with regularization parameter ρ^{-1}, the inverse of the signal-to-noise ratio (SNR) $\rho = b_0/N_0$ for the adopted white observation noise model, $\mathbf{R}_{\mathbf{N}} = N_0\mathbf{I}$ with intensity N_0. In that case, the robust smoothing window

$$\mathbf{W} = \mathbf{\Omega} = (w_0\mathbf{I} + \mathbf{M})^{-1} \quad (23)$$

is completely defined by the matrix $\mathbf{M}$ that induces the metrics structure in the solution space [6] with the scaling factor $w_0 = \text{tr}\{\mathbf{S}^{+}\mathbf{F}^{+}\mathbf{F}\mathbf{S}\}/K$. Such robustified $\mathbf{W}$ can be pre-computed a priori for a family of different admissible ρ as it was proposed in the previous studies [7]. Here, we employ a practical constraints of high SNR operational conditions [22], $\rho >> 1$, in which case one can neglect also the constant bias $\mathbf{Z} = Z_0\mathbf{I}$ in (16) because it does not affect the pattern of the SSP estimate. Following these practically motivated assumptions, the resulting RBR estimator for the SSP becomes

$$\hat{\mathbf{B}}_{RBR} = \mathbf{B}_0 + \mathbf{\Omega}\mathbf{V}, \quad (24)$$

where $\mathbf{V} = \{\mathbf{F}\mathbf{U}\mathbf{U}^{+}\mathbf{F}^{+}\}_{\text{diag}}$ represents now the robust SS vector.

B. Matched spatial filtering (MSF) algorithm

The simplest rough SSP and RSS estimators can be constructed as further simplification of (24) if the trivial a priori model information ($\mathbf{P}_{\mathbf{W}} = \mathbf{I}$ and $\mathbf{B}_0 = b_0\mathbf{I}$) is adopted,

and roughly approximate the SS formation operator **F** by the adjoint SFO, i.e. the matched filter

$$\mathbf{F} \approx \gamma_0 \mathbf{S}^{+} \tag{25}$$

where the normalizing constant γ_0 provides balance of the operator norms $\gamma_0^2 = \mathrm{tr}^{-1}\{\mathbf{S}^{+}\mathbf{S}\mathbf{S}^{+}\mathbf{S}\}\mathrm{tr}\{\mathbf{F}\mathbf{S}\mathbf{S}^{+}\mathbf{F}^{+}\}$. Equation (24) is simplified to its rough matched spatial filter (MSF) version

$$\hat{\mathbf{B}}_{MSF} = \mathbf{\Omega}\mathbf{\Pi}, \tag{26}$$

where the rough SS, $\mathbf{\Pi} = \gamma_0^2 \{\mathbf{S}^{+}\mathbf{U}\mathbf{U}^{+}\mathbf{S}\}_{\mathrm{diag}}$, is now formed applying the adjoint operator $\mathbf{S}^{+}$, and the windowing of the rough SS $\mathbf{\Pi}$ is performed applying the smoothing filter $\mathbf{\Omega} = (w_0\mathbf{I} + \mathbf{M})^{-1}$ with the nonnegative entry [7]. Equation (26) is referred to as matched spatial filtering (MSF) algorithm for estimation of the SSP. Equation (26) is recognized to be a vector-form representation of the conventional kernel SSP estimation algorithm [24], in which the SS is formed as the squared modulus of the outcomes of the matched spatial filter applied to the recorded data signal. Thus, in the framework of the BR inference-based approach to RS imaging [6], the traditional MSF technique (26) can be viewed as a rough simplified version of the RBR algorithm.

IV. Quality Metrics

The traditional quantitative quality metric [1] for RS images is the so-called Improvement in the Output Signal to Noise Ratio (IOSNR), which provides the metrics for performance gains attained with different employed estimators in dB scale

$$IOSNR(dB) = 10 \cdot \log_{10}\left(\frac{\sum_{k=1}^{K}\left(\hat{b}_k^{(MSF)} - b_k\right)^2}{\sum_{k=1}^{K}\left(\hat{b}_k^{(p)} - b_k\right)^2} \right), \quad p = 1,...,P, \tag{27}$$

where b_k represents the value of the k-th element of the original SSP, $\hat{b}_k^{(MSF)}$ represents the value of the k-th element of the rough SSP estimate formed applying the matched spatial filtering (MSF) method, and $\hat{b}_k^{(p)}$ represents the value of the k-th element of the enhanced SSP estimate formed applying the pth enhanced imaging method ($p = 1,\ldots,P$), respectively.

The percentage IOSNR (PIOSNR) quality metric is a modification of the IOSNR metric [22]; it expresses the percentage of the gained reconstruction improvement specified as follows

$$PIOSNR(\%) = 100\left(1 - \frac{\sum_{k=1}^{K}\left(\hat{b}_k^{(p)} - b_k\right)^2}{\sum_{k=1}^{K}\left(\hat{b}_k^{(MSF)} - b_k\right)^2} \right), \quad p = 1,...,P. \tag{28}$$

The total Mean Square Error (MSE) is defined as [24]

$$MSE = \sum_{k=1}^{K}\left(\hat{b}_k^{(p)} - b_k\right)^2, \quad p = 1,...,P. \tag{29}$$

The quality metrics specified by (27) thru (29) allow to quantify the performances of the employed SSP reconstructive estimation methods (enumerated by p = 1,…,P).

V. Simulations

The simulation experiment is performed for test (artificially synthesized) scenes applying the partially synthesized aperture as an RS imaging system [8]. The SFO of all RS images is factorized along two axes in the image plane: the azimuth (horizontal axis, x_1) and the range (vertical axis, x_2). Following the common practically motivated technical considerations [5] we modelled a triangular shape of the range ambiguity function (AF) $\Psi_r(x_2)$ in the x_2 direction, and a $|sinc|^2$ shape of the azimuth AF $\Psi_a(x_1)$ in the x_1 direction at the zero crossing level with fractionally synthesized array.

The behavior and performance indices of the described estimators are examined for a RS system configuration applied to two test scenes.

In the first simulation scenario, the assigned values of the AF widths are: 5 pixels width for $\Psi_r(x_2)$ and 10 pixels width for $\Psi_a(x_1)$. In the simulations reported in Fig. 1, we considered the case of white Gaussian observation noise with the SNR of 30 dB. Figure 1(a) shows the 1000×1000-pixel original synthesized test scene. Figure 1(b) reports the image formed implementing the MSF method. Figure 1(c) presents the reconstructed (enhanced) synthesized image formed using the BR estimator. Last, Figure 1(d) shows the reconstructed (enhanced) synthesized image formed using the RBR estimator. The quantitative quality metrics of the *IOSNR*, *PIOSNR* and *MSE* gained with the employed enhanced imaging methods for the simulated fractional aperture synthesis scenarios with different levels of noise are reported in Table 1.

In the second simulation scenario, the high-resolution real-world geophysical image is used as test scene [4]. The tested 1000×1000-pixel original geophysical scene is shown in Fig. 2(a). The simulation experiment is applied with the following system-level specifications: 5 pixels width for $\Psi_r(x_2)$ and 20 pixels width for $\Psi_a(x_1)$, respectively.

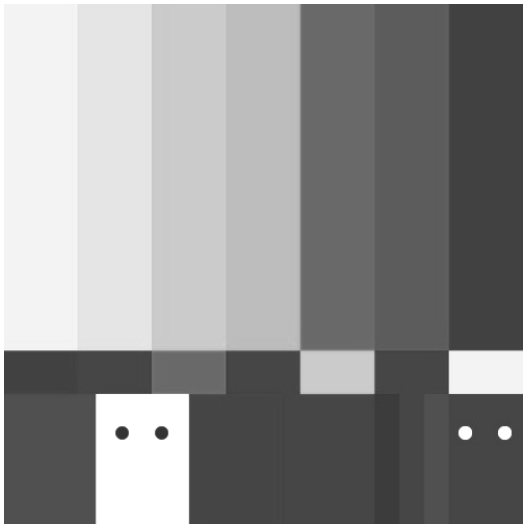

a. Original artificially synthesized test scene.

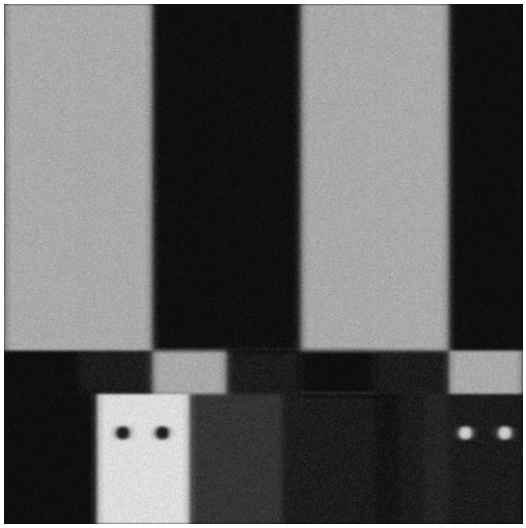

b. Low-resolution scene image formed applying the MSF method.

c. Test scene reconstruction using the BR estimator.

d. Test scene reconstruction using the RBR estimator.

Figure 1. Simulation results of the synthesized test scene SSP reconstruction. Specifications of the simulation experiment are summarized in Table 1.

TABLE 1

COMPARATIVE TABLE OF THE QUALITY METRICS GAINED WITH DIFFERENT ESTIMATION METHODS FOR THREE LEVELS OF NOISE (SNR). RESULTS ARE REPORTED FOR THE SYNTHESIZED TEST SCENE.

SYSTEM SPECIFICATIONS: RANGE TRIANGULAR SHAPE OF AF $\Psi_R(X_2) = 5$ PIXELS WIDTH; AZIMUTH $|SINC|^2$ SHAPE OF AF $\Psi_A(X_1) = 10$ PIXELS WIDTH.

	Method →	**MSF**			**BR**			**RBR**		
	SNR [dB] →	**20**	**25**	**30**	**20**	**25**	**30**	**20**	**25**	**30**
Metrics	**IOSNR [dB]**	15.65	20.84	25.23	10.26	14.76	17.37	11.16	15.53	18.36
	PIOSNR (%)	72.34	78.16	77.06	92.82	92.75	95.54	91.73	91.43	94.33
	MSF	0.20	0.50	0.60	0.03	0.20	0.10	0.04	0.22	0.14

a. Original artificially synthesized test scene.

b. Low-resolution scene image formed applying the MSF method.

c. Test scene reconstruction using the BR estimator.

d. Test scene reconstruction using the RBR estimator.

Figure 2. Simulation results of the real-world geophysical scene with SSP reconstruction. Specifications of the simulation experiment are summarized in Table 2.

TABLE 2

COMPARATIVE TABLE OF THE QUALITY METRICS GAINED WITH DIFFERENT ESTIMATION METHODS FOR THREE LEVELS OF NOISE (SNR). RESULTS ARE REPORTED FOR THE GEOPHYSICAL SCENE.

SYSTEM SPECIFICATIONS: RANGE TRIANGULAR SHAPE OF AF $\Psi_R(X_2) = 5$ PIXELS WIDTH; AZIMUTH $|SINC|^2$ SHAPE OF AF $\Psi_A(X_1) = 20$ PIXELS WIDTH.

	Method →	**MSF**			**BR**			**RBR**		
	SNR [dB] →	**15**	**20**	**25**	**15**	**20**	**25**	**15**	**20**	**25**
Metrics	**IOSNR [dB]**	10.15	15.32	20.25	5.47	9.85	12.63	6.15	10.62	13.04
	PIOSNR (%)	81.37	86.62	85.24	96.63	91.68	99.10	95.18	90.29	98.24
	MSF	0.16	0.46	0.57	0.02	0.24	0.24	0.03	0.29	0.34

TABLE 3
OPERATIONS PER CYCLE USED ON THE COMPUTATIONAL IMPLEMENTATION OF DIFFERENT SSP RECONSTRUCTION METHODS.

Method	Equation	Processing Algorithm		Operations per cycle
BR	(21)	$\hat{\mathbf{B}}_{BR} = \mathbf{B}_P + \mathbf{P}\mathbf{B}_0 + \mathbf{W}(\hat{\mathbf{B}})\{\mathbf{V}(\hat{\mathbf{B}}) - \mathbf{Z}(\hat{\mathbf{B}})\}$	→	$\boldsymbol{K} + \boldsymbol{K}^{(2)} + \boldsymbol{K}^{(4)}\boldsymbol{I}$
RBR	(24)	$\hat{\mathbf{B}}_{RBR} = \mathbf{B}_0 + \boldsymbol{\Omega}\mathbf{V}$	→	$\boldsymbol{K} + \boldsymbol{K}^{(2)} \cdot \boldsymbol{I}$
MSF	(16)	$\hat{\mathbf{B}}_{MSF} = \boldsymbol{\Omega}\boldsymbol{\Pi}$	→	$\boldsymbol{K} \cdot \boldsymbol{I}$

TABLE 4
PROCESSING TIMES CONSUMED FOR DIFFERENT SSP RECONSTRUCTION METHODS. THE RESULTS ARE REPORTED IN SECONDS.
NOTE – PROCESSING TIMES ARE CALCULATED CONSIDERING ALL THE CPU CLOCK SPEED IS DEDICATED; RESULTS MAY VARY DEPENDING ON THE PROCESSOR TYPE.

Method	Operation per cycle	Total operations	PC Time [seconds]	WS Time [seconds]	DH Time [seconds]
BR	$\boldsymbol{K} + \boldsymbol{K}^{(2)} + \boldsymbol{K}^{(4)}\boldsymbol{I}$	$3.48\text{x}10^{13}$	$1.30\text{x}10^{4}$	$9.15\text{x}10^{3}$	$11.60\text{x}10^{3}$
RBR	$\boldsymbol{K} + \boldsymbol{K}^{(2)} \cdot \boldsymbol{I}$	$6.92\text{x}10^{10}$	26.15	18.21	230.66
MSF	$\boldsymbol{K} \cdot \boldsymbol{I}$	$1.34\text{x}10^{8}$	0.05	0.035	0.45

In the basic simulations, we considered the case of white Gaussian observation noise with the SNR of 30 dB. Figure 2(b) show the image formed via implementing the MSF method with the system parameters specified in the figure captions. Figure 2(c) present the reconstructed (enhanced) images formed using the BR estimator. Figure 2(d) show the enhanced image reconstructed with the RBR method. The quantitative quality metrics of the *IOSNR*, *PIOSNR* and *MSE* gained with different tested enhanced imaging methods for the simulated aperture synthesis scenario with different levels of noise are reported in Table 2.

VI. COMPUTATIONAL COMPLEXITY

Real-time computing is traditionally referred to as study of software systems which are subject to some real-time operational constraints [1]. By contrast, a non-real-time system is one where there is no deadline, even if fast response or high performance is desired or preferred [1], [19]. The needs of real-time software are often addressed in the context of real-time operating systems [1], and synchronous programming languages [2], which provide frameworks on which to build up the real-time application software [2], [3].

A real time RS data processing system is one, which performances can be considered (within a particular RS context) to be mission critical [3]. Real-time computations can be said to have failed if they are not completed before their deadline, where the deadline is relative to an RS event [19]. A real-time deadline must be met, regardless of system load [1].

For the previously described image enhancement and SSP mapping methodologies, it is reasonable to define the computational complexity via determining the number of computational operations needed to perform the particular employed algorithms [10]. Consider $\boldsymbol{K}$ as a matrix, $\boldsymbol{I}$ as an inverse matrix. Let suffix n represents the number of matrix multiplications and/or inversions required to complete the mathematical operations (e.g., $\boldsymbol{K}^{(4)}$ represents a quadruple matrix multiplication, $\boldsymbol{I}^{(2)}$ represents a double matrix inversion, etc.). For the particular employed simulation formats, $\boldsymbol{K}$ and $\boldsymbol{I}$ are 1000×1000 matrixes. The number of operations needed to complete one reconstruction cycle for the tested and compared methods are reported in Table 3. With these results, one can analyze the processing time (in operation cycles) needed to perform computationally each employed algorithm.

Table 4 reports the computational times required for completing the compared SSP reconstructive techniques with three different typical computer processing unit (CPU) clock speeds: (i) with a personal computer (PC) running at 2.66 GHz with a single processor; (ii) with a workstation (WS) running at 3.80 GHz with a duo processor, and (iii) with a dedicated hardware (DH) running at 300 MHz with a single processor.

The presented results of comparative simulation analysis illustrate the behavior and overall imaging performance improvements gained with the RBR approach compared with other methods in both the reconstruction quality metrics and computational complexity reduction.

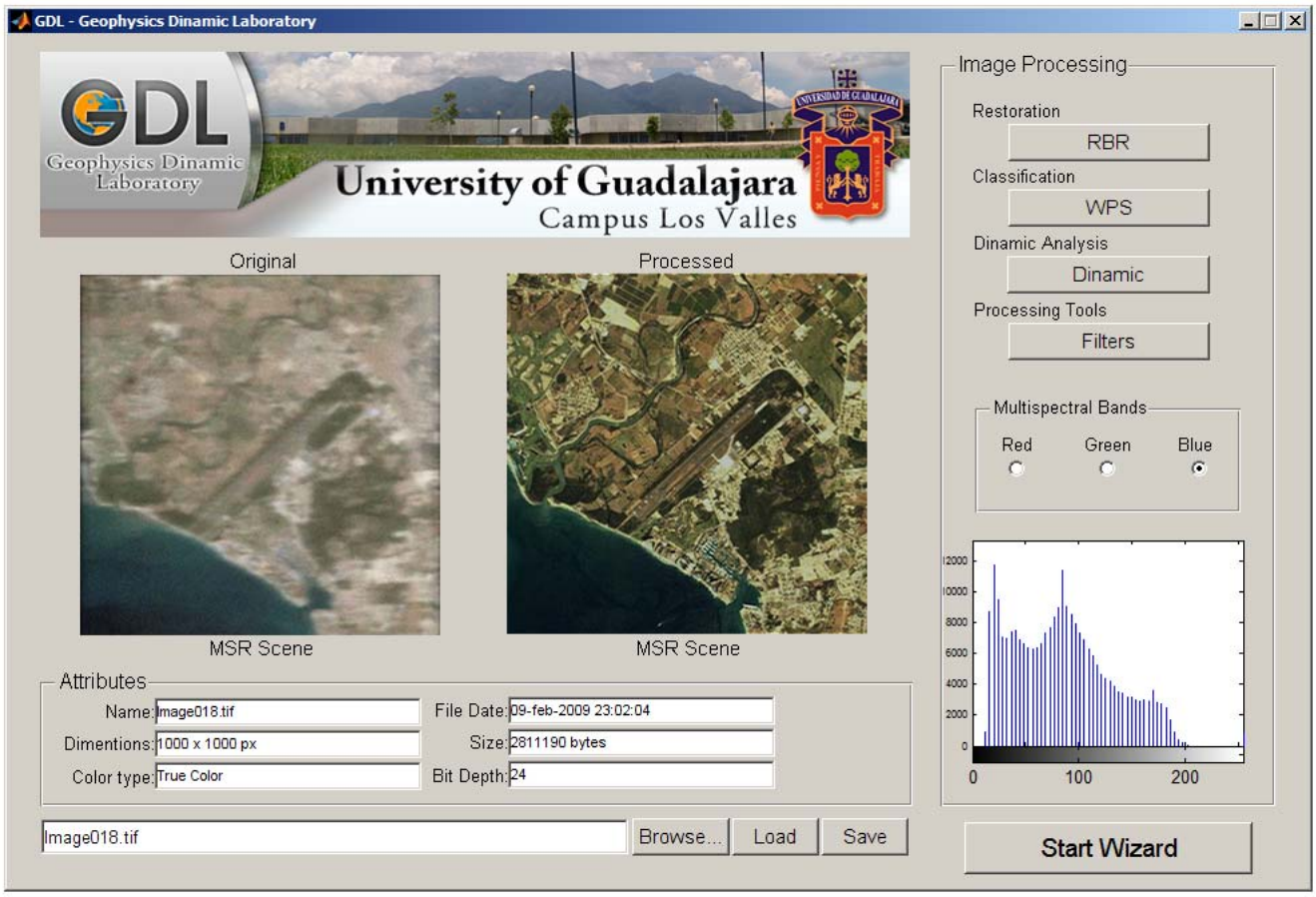

Figure 3. Graphic interface of the virtual GDL intelligent software.

The advantages of the well designed robust imaging experiments (RBR method) over the cases of poorer designed experiments (MSF algorithm) were investigated through extensive simulation study and reported here for different multi-grade test scenes.

VII. Geophysics Dynamic Laboratory

An innovative algorithmic proposition is the Geophysics Dynamic Laboratory (GDL) software that provides a friendly end-user application for different MRS imaging problems in the context of intelligent experiment design paradigm. The scientific challenge is to develop and investigate via the GDL an intelligent signal processing perspective for collaborative RS data acquisition, adaptive processing and information fusion for the purposes of high-resolution RS imaging, search, discovery, discrimination, mapping and problem-oriented analysis of spatially distributed physical remote sensing signature fields. Figure 3 shows the graphical user interface of the GDL software.

The end-user oriented GDL software will be elaborated directly to assist in system level and algorithmic level optimization of such multi-sensor collaborative image formation, enhancement, fusion and post-processing tasks performed via RS imagery.

The GDL software aggregates interactive computational tools that offer different options of acquisition and processing of images in JPEG, TIFF and PNG formats as input scenes, application of different levels of image degradation with a particular simulated MRS system, simulation of random noising effects with different noise intensities and distributions.

Moreover, MRS image enhancement, fusion, reconstruction segmentation, classification, quantification and dynamical post-processing methodologies can be simulated.The computational implementation for different MRS imaging problems in the context of intelligent experiment design paradigm via the GDL software is a matter of further studies.

VIII. Concluding Remarks

We have performed the detailed comparative study of different proposed robust numerical versions of the high-resolution adaptive remote sensing imaging method: the BR technique. The performed comparative analysis of the computational complexities of different imaging techniques based on the robust SSP and RSS estimators revealed that the BR-related robust imaging algorithms manifest user-controlled real-time implementation performances because the RS deadline event is completed in each stage of the image reconstruction process to provide the system response in a virtually "real" (i.e., user-required) time.

In the RS applications related to the real-world 1000×1000-pixel geophysical scene image reconstruction scenario, the computational complexity for performing the enhanced RS imaging with the proposed RBR algorithm in comparison with the original BR method was drastically decreased, i.e., approximately 10^5 times and required 27 seconds of the overall computational time. Also, the simulation protocols reported for different tested scenarios verify in more details the substantial efficiency of the proposed MRS imaging technique.

Acknowledgment

The authors would like to thank the "Programa de Mejoramiento del Profesorado PROMEP" of the Public Education Secretary (SEP) of Mexico and the University of Guadalajara for the resources provided for this research under the research project number PROMEP/103.5/08/2919 and titled "Agregación de métodos para el mapeo y caracterización del medio ambiente mediante técnicas de percepción remota".

References

[1] P.M. Mather, Computer processing of remotely-sensed images, John Wiley & Sons, U.S.A., 2004.

[2] E. Schrödinger, Science, theory and man, Dover, U.S.A., 1957.

[3] S. Greenfield, The human brain: a guided tour, Weinfeld and Nicholson, U.K., 1997.

[4] T. Freeman, Jet Propulsion Laboratory, Space Imaging, "What is imaging radar?", 2005, http://www.spaceimaging.com.

[5] C. Olmsted, Scientific SAR user's guide, Alaska SAR Facility, U.S.A. 1993.

[6] Y.V. Shkvarko, "Estimation of Wavefield Power Distribution in the Remotely Sensed Environment: Bayesian Maximum Entropy Approach", IEEE Transactions on Signal Processing, vol. 50, pp. 2333-2346, September 2002.

[7] Y.V. Shkvarko, "Unifying Regularization and Bayesian Estimation Methods for Enhanced Imaging with Remotely Sensed Data. Part I – Theory", IEEE Transactions on Geoscience and Remote Sensing, vol. 42, pp. 923-931, March 2004.

[8] Y.V. Shkvarko, "Unifying Regularization and Bayesian Estimation Methods for Enhanced Imaging with Remotely Sensed Data. Part II – Implementation and Performance Issues", IEEE Transactions on Geoscience and Remote Sensing, vol. 42, pp. 932-940 , March 2004.

[9] F.M. Henderson and A.V. Lewis, Principles and application of imaging radar, manual of remote sensing, John Wiley & Sons, U.S.A., 1998.

[10] J.L. Starck, F. Murtagh and A. Bijaoui, Image processing and data analysis, the multiscale approach, Cambridge University Press, U.K., 1998.

[11] B.R. Mahafza, Radar systems analysis and design using MATLAB, CRC Press, U.S.A., 2000.

[12] A.W. Doerry, F.M. Dickey, L.A. Romero and J.M. DeLaurentis, "Difficulties in Superresolving SAR Images", SPIE Proceedings, vol. 4727, pp. 122-133, April 2002.

[13] R.C. Puetter, "Information Language and Pixon-based Image Reconstruction", SPIE Proceedings, vol. 2827, pp. 12-31, 1996.

[14] S. Haykin and A. Steinhardt, Adaptive radar detection and estimation, John Wiley & Sons, U.S.A., 1992.

[15] D.C. Bell and R.M. Narayanan, "Theoretical Aspects of Radar Imaging using Stochastic Waveforms", IEEE Transactions on Signal Processing, vol. 49, pp. 349-400, February 2001.

[16] Y.V. Shkvarko, "Theoretical Aspects of Array Radar Imaging via Fusing Experiment Design and Descriptive Regularization Techniques", Proceedings of the 2nd IEEE Workshop on Sensor Array and Multichannel Signal Processing, Washington U.S.A., 2002.

[17] GeoEye – Innovative Geospatial Products and Solutions, 2009, http://www.geoeye.com.

[18] R.O. Harger, Synthetic aperture radar systems: theory and design, Academic Press, U.S.A. 1970.

[19] R. Bamler, "A Comparison of Range-Doppler and Wave-Number Domain SAR Focusing Algorithms", IEEE Transactions on Geoscience and Remote Sensing, vol. 30, pp. 706-713, June 1991.

[20] S.E. Falkovich, V.I. Ponomaryov and Y.V. Shkvarko, Optimal spatial-temporal signal processing for spread radio channels, Radio and Communication Press, USSR 1989.

[21] G. Franceschetti and R. Lanari, Synthetic aperture radar processing, Boca Raton, FL: CRC, 1999.

[22] S.A. Hovanessian, Introduction to sensor systems, Norwood, MA: Artech House, 1988.

[23] L.G. Cutrona, "Synthetic Aperture Radar", in Radar handbook, McGraw-Hill, 1990.

[24] D.R. Wehner, High-resolution radar, Artech House, 1994.

[25] Y.V. Shkvarko and I. Villalon-Turrubiates, "Remote Sensing Imagery and Signature Fields Reconstruction via Aggregation of Robust Regularization with Neural Computing", in Advanced Concepts for Intelligent Vision Systems, J. Blanc-Talon, W. Philips, D. Popescu and P. Scheunders, Ed. Germany: Springer-Verlag, pp. 865-876, August 2007.

[26] I.E. Villalon-Turrubiates and Y.V. Shkvarko, "Comparative Study of the Descriptive Experiment Design and Robust Fused Bayesian Regularizarion Techniques for High-Resolution Radar Imaging", Scientific and Technical Journal on Radioelectronics and Informatics, vol. 1, no. 1, pp. 34-48, 2008.

[27] Y.V. Shkvarko, I. Villalon-Turrubiates and J.L. Leyva-Montiel, "Remote Sensing Signature Fields Reconstruction via Robust Regularization of Bayesian Minimum Risk Technique", in Proceedings of the 2nd IEEE International Workshop on Computational Advances in Multi-Sensor adaptive processing, Virgin Islands U.S.A., pp. 237-240, December 2007.